

# Collisional Transfer of Atomic Coherence

Joseph Goldfrank

College of William and Mary, Dept. of Physics

11 May 2009

# 1 Introduction

## 1.1 Motivation

Quantum information storage is one of the major requirements to implement useful quantum computation and communication. To be of use in the physical implementation of quantum computer networks, a storage mechanism must be readily able to interconvert between stored information and transmitted information.[1] Such a mechanism is one of the major challenges in the development of quantum communications. Quantum optical systems are well-suited to this application. They couple photons, the method of choice for quantum information transmission[1], and atomic ensembles, which provide a reliable and long-lived method by which to store quantum information[2].

As discussed by Fleischauer et al.[2], and implemented by Julsgaard, et al.[3] storage and retrieval of quantum information in atomic ensembles using electromagnetically induced transparency is physically feasible, although at this point the storage time, which is of particular import for use with quantum communications, has been limited by spin-wave decay[4]. Indeed, current light storage experiments limit the pulse width and storage time such that the effects of spin-wave decoherence are negligible, which has limited storage time to the order of  $100\mu\text{s}$ . For quantum memory applications, it is desirable that this storage time be increased. Decoherence time, and thus light storage time, can be extended through mitigation of various relaxation mechanisms[6], namely wall and spin-exchange collisions, which is the focus of this research. If there

is a demonstrated increase in decoherence time through collisional transfer, it may be possible in the future to extend storage time further through collisional transfer of coherence to and from atoms with much longer coherence lifetime than Rb.

## 1.2 Introduction to the Experiment

This research builds on previous research on storage of light in ensembles of radiators using electromagnetically induced transparency (EIT). EIT uses an optical field to make a previously opaque medium transparent to a second, "signal" field of specific polarization and frequency[7]. Changes in the control field allow the quantum information in the signal pulse to be coherently and reversibly mapped to the atoms in the medium, however the storage time is limited by the atomic coherence lifetime[8].

The current technique for light storage with EIT utilizes a  $\Lambda$ -system of Rb hyperfine levels, specifically the  $5\ ^2S_{\frac{1}{2}}F=2 \rightarrow 5^2P_{\frac{1}{2}}F'=2$  and  $5\ ^2S_{\frac{1}{2}}F=1 \rightarrow 5^2P_{\frac{1}{2}}F'=2$  transitions[4]. As we are investigating various mechanisms to reduce the decay rate rather than actually storing light, we will utilize Zeeman sublevels rather than hyperfine levels. We will replicate the procedure of Sautenkov, et al. 2000[10] ( which made use of EIT using a  $\Lambda$ -system derived from Zeeman sublevels) to enhance the nonlinear Faraday effect (rotation of linear polarization of an optical field propagated through a medium). The nonlinear Faraday effect relies on the same coherent state associated with EIT that is used in light storage. As the physical setup required to observe polarization rotation using Zeeman sublevels is much simpler than that re-

quired to store light utilizing hyperfine levels, this method is well-suited to our uses. We will also introduce a second laser on a different Rb transition in order to observe the effect on the polarization rotation of the laser on the first transition. Our goal is to observe some effect on polarization rotation that can be attributed to collisional transfer of coherence and the subsequent effective reduction in decay time.

## 2 Relevant Theory

### 2.1 Density Matrix Formalism

A complete theoretical treatment of nonlinear Faraday rotation using the Zeeman sublevels of  $^{85}\text{Rb}$  and  $^{87}\text{Rb}$  is complicated and beyond the scope of this work. It is useful, however, to mathematically characterize polarization rotation using a simple 3-level system. We will mathematically describe a system whereby a linearly polarized electromagnetic field propagates through a vapor cell near a (single and isolated) atomic transition, with an applied magnetic field creating a three-level system between the ground state and the Zeeman sublevels of the excited state. This mimics the manner in which the Zeeman sublevels are split in our experimental setup.

The linearly polarized field is treated, as two opposite circularly-polarized fields,  $\Omega_+$  and  $\Omega_-$ . Thus an incident wave propagating along  $\hat{z}$  and linearly polarized along  $\hat{x}$  can be described as follows:

$$\tilde{E}(z, t) = E_0 e^{i(kz - \omega t)} \hat{x} = E_0 e^{i(kz - \omega t)} \hat{x} + \frac{E_0}{\sqrt{2}} e^{i(kz - \omega t + \frac{\pi}{2})} \hat{y} + \frac{E_0}{\sqrt{2}} e^{i(kz - \omega t - \frac{\pi}{2})} \hat{y} = \frac{1}{\sqrt{2}} E_+ + \frac{1}{\sqrt{2}} E_- \quad (1)$$

with  $E_+$  and  $E_-$  being defined as

$$E_+(z, t) = \frac{E_0}{\sqrt{2}} e^{i(kz - \omega t)} \hat{x} + \frac{E_0}{\sqrt{2}} e^{i(kz - \omega t + \frac{\pi}{2})} \hat{y} \quad (2)$$

$$E_-(z, t) = \frac{E_0}{\sqrt{2}} e^{i(kz - \omega t)} \hat{x} + \frac{E_0}{\sqrt{2}} e^{i(kz - \omega t - \frac{\pi}{2})} \hat{y} \quad (3)$$

The three-state system with ground state  $a$  and excited states  $b_+$  and  $b_-$  can be described by the wave function:

$$|\Psi\rangle = \alpha|a\rangle + \beta_+|b_+\rangle + \beta_-|b_-\rangle \quad (4)$$

In order to describe coherences and decays, it is necessary to use density-matrix formalism. While the mathematics of density-matrix formalism are outside the scope of this thesis, quantities derived therefrom permit us to calculate the effect on a CW EM field propagating through a vapor cell on resonance with an approximate three-level system described by the density matrix.

$$\hat{\rho} = |\Psi\rangle\langle\Psi| = \begin{pmatrix} |\alpha|^2 & \alpha\beta_+^* & \alpha\beta_-^* \\ \beta_+\alpha^* & |\beta_+|^2 & \beta_+\beta_-^* \\ \beta_-\alpha^* & \beta_-\beta_+^* & |\beta_-|^2 \end{pmatrix} \quad (5)$$

Where  $\rho_{aa}$ ,  $\rho_{b_+b_+}$ , and  $\rho_{b_-b_-}$  are simply the populations of the different states.  $\rho_{ab\pm}$  govern changes in optical fields propagating through the cell, and  $\rho_{b_{\pm}b_{\mp}}$  represents the ground-state Zeeman coherence. For steady-state fields, changes in the Rabi frequencies  $\Omega_{\pm}$  corresponding to fields  $E_{pm}$  are described by:

$$\frac{\partial\Omega_{\pm}}{\partial z} = i\kappa_{ab}\rho_{ab\mp} \quad (6)$$

where coupling constant  $\kappa = \frac{3}{8\pi}N\lambda^2\gamma_{ab}$  ; with  $\gamma_{ab}$  the spontaneous decay rate between states  $|a\rangle$  and  $|b_{\pm}\rangle$

The Von-Neumann equation  $i\hbar\frac{\partial\hat{\rho}}{\partial t} = [\hat{H}, \hat{\rho}]$  allows the time-evolution of the elements of the density matrix to be described. Thus the time evolution of  $\rho_{ab\pm}$  (the optical polarizations) and  $\rho_{b-b+}$  (the ground state coherence) respectively are

$$\dot{\rho}_{ab\pm} = -\Gamma_{ab\pm}\rho_{ab\pm} + i\Omega_{\mp}(\rho_{b\pm b\pm} - \rho_{aa}) + i\Omega_{\pm}\rho_{b\mp b\pm} \quad (7)$$

$$\dot{\rho}_{b-b+} = -\Gamma_{b-b+}\rho_{b-b+} + i\Omega_{+}^*\rho_{ab+} - i\Omega_{-}\rho_{b-a} \quad (8)$$

Where we have introduced phenomenological decays  $\Gamma_{ab\pm} = \gamma + i\Delta$  and  $\Gamma_{b-b+} = \gamma_0 + 2i\delta$ ,  $\Delta$  being the one-photon detuning and  $\delta$  the two-photon detuning.  $\gamma$ , the decay rate for polarizations  $\rho_{ab}$  is the spontaneous emission rate for Rb atoms.  $\gamma_0$  is the ground state coherence decay rate; as ground-state coherence is much longer-lived  $\gamma_0 \ll \gamma$ .

## 2.2 Polarization Rotation

As our EM fields are entirely in the steady-state regime, there is no time evolution, which implies that:

$$\dot{\rho}_{ab\pm} = \dot{\rho}_{b-b+} = 0 \quad (9)$$

and thus equations (7) and (8) can now be written:

$$-\Gamma_{ab\pm}\rho_{ab\pm} + i\Omega_{\mp}(\rho_{b\pm b\pm} - \rho_{aa}) + i\Omega_{\pm}\rho_{b\mp b\pm} = 0 \quad (10)$$

$$-\Gamma_{b-b+}\rho_{b-b+} + i\Omega_{+}^*\rho_{ab+} - i\Omega_{-}\rho_{b-a} = 0 \quad (11)$$

solving equation (10) for  $\rho_{ab\pm}$ , assuming  $(\rho_{b\pm b\pm} - \rho_{aa}) = \frac{1}{2}$  (given roughly even population distribution between  $(\rho_{b+b+})$  and  $(\rho_{b-b-})$  and no population in the excited state) yields:

$$\rho_{ab\pm} = \frac{\frac{1}{2}i\Omega_{\mp} + i\Omega_{\pm}\rho_{b\mp b\pm}}{\Gamma_{ab\pm}} \quad (12)$$

and by substituting the result (12) into equation (11), and expression for  $\rho_{b-b+}$  is developed:

$$\rho_{b-b+} = \frac{-\frac{1}{2}\Omega_{+}^*\Omega_{-}\left(\frac{1}{\Gamma_{ab+}} + \frac{1}{\Gamma_{b-a}}\right)}{\frac{|\Omega_{+}|^2}{\Gamma_{ab+}} + \frac{|\Omega_{-}|^2}{\Gamma_{b-a}} - \Gamma_{b-b+}} \quad (13)$$

substituting (13) into (12) yields

$$\rho_{ab+} = i\Omega_{-}\frac{1}{2\Gamma_{ab+}}\frac{\frac{|\Omega_{-}|^2}{\Gamma_{b-a}} - \frac{|\Omega_{+}|^2}{\Gamma_{b-a}} + \Gamma_{b-b+}}{\frac{|\Omega_{-}|^2}{\Gamma_{b-a}} + \frac{|\Omega_{+}|^2}{\Gamma_{ab+}} + \Gamma_{b-b+}} \quad (14)$$

and it can now be seen that, combining equations (14) and (6):

$$\frac{\partial \Omega_{\pm}}{\partial z} = -\kappa \Omega_{\pm} \frac{1}{2\Gamma_{ab+}} \frac{\frac{|\Omega_-|^2}{\Gamma_{b-a}} - \frac{|\Omega_+|^2}{\Gamma_{b-a}} + \Gamma_{b-b+}}{\frac{|\Omega_-|^2}{\Gamma_{b-a}} + \frac{|\Omega_+|^2}{\Gamma_{ab+}} + \Gamma_{b-b+}} \quad (15)$$

given that each polarization undergoes a phase shift and amplitude attenuation as it propagates through the vapor cell,  $\Omega_{\pm}(z)$  can be described by

$$\Omega_{\pm}(z) = \Omega_0 e^{i\phi_{\pm}(z)} e^{-\alpha_{\pm} z} \quad (16)$$

and differentiating:

$$\frac{\partial \Omega_{\pm}}{\partial z} = \Omega_{\pm}(z) (-\alpha_{pm} + ikn_{pm}) \quad (17)$$

comparing to our result in equation (15) yields

$$\alpha_{\pm} = \kappa Re \left( \frac{1}{2\Gamma_{ab+}} \frac{\frac{|\Omega_-|^2}{\Gamma_{b-a}} - \frac{|\Omega_+|^2}{\Gamma_{b-a}} + \Gamma_{b-b+}}{\frac{|\Omega_-|^2}{\Gamma_{b-a}} + \frac{|\Omega_+|^2}{\Gamma_{ab+}} + \Gamma_{b-b+}} \right) \quad (18)$$

$$kn_{\pm} = -\kappa Im \left( \frac{1}{2\Gamma_{ab+}} \frac{\frac{|\Omega_-|^2}{\Gamma_{b-a}} - \frac{|\Omega_+|^2}{\Gamma_{b-a}} + \Gamma_{b-b+}}{\frac{|\Omega_-|^2}{\Gamma_{b-a}} + \frac{|\Omega_+|^2}{\Gamma_{ab+}} + \Gamma_{b-b+}} \right) \quad (19)$$

We can now estimate both the absorption and polarization rotation of the field as it propagates through the vapor cell, noting that total absorption is proportional to  $\alpha_+ + \alpha_-$  but rotation is proportional to  $\left(\frac{kn_+ - kn_-}{2}\right)$  resulting from  $kn_+$  and  $kn_-$  acting on opposite circular polarizations  $\Omega_+$  and  $\Omega_-$  (from equations (2) and (3)).

$$\Omega_{\pm}(z, t) = \frac{E_0}{2} e^{i(kz - \omega t)} \hat{x} + \frac{E_0}{2} e^{i(kz - \omega t \pm \frac{\pi}{2})} \hat{y} \quad (20)$$

when phase shifted by  $\pm\phi = kn_{\pm}$  becomes:

$$\Omega_{\pm}(z, t) = \frac{E_0}{\sqrt{2}} e^{i(kz - \omega t \pm \phi)} \hat{x} + \frac{E_0}{\sqrt{2}} e^{i(kz - \omega t \pm \frac{\pi}{2} \pm \phi)} \hat{y} \quad (21)$$

and recombining into a linear polarization yields:

$$\tilde{E}(z, t) = \Omega_+ + \Omega_- = \frac{E_0}{\sqrt{2}} e^{i(kz - \omega t)} (e^{i\phi} + e^{-i\phi}) \hat{x} + \frac{E_0}{\sqrt{2}} e^{i(kz - \omega t)} (e^{i\frac{\pi}{2} + i\phi} + e^{i\frac{\pi}{2} - i\phi}) \hat{y} \quad (22)$$

which through complex trigonometric identity is equivalent to:

$$\tilde{E}(z, t) = \frac{E_0}{\sqrt{2}} e^{i(kz - \omega t)} \cos \phi \hat{x} + \frac{E_0}{\sqrt{2}} e^{i(kz - \omega t)} \sin \phi \hat{y} \quad (23)$$

which is clearly the incident polarization rotated by angle  $\phi = \frac{kn_+ - kn_-}{2}$

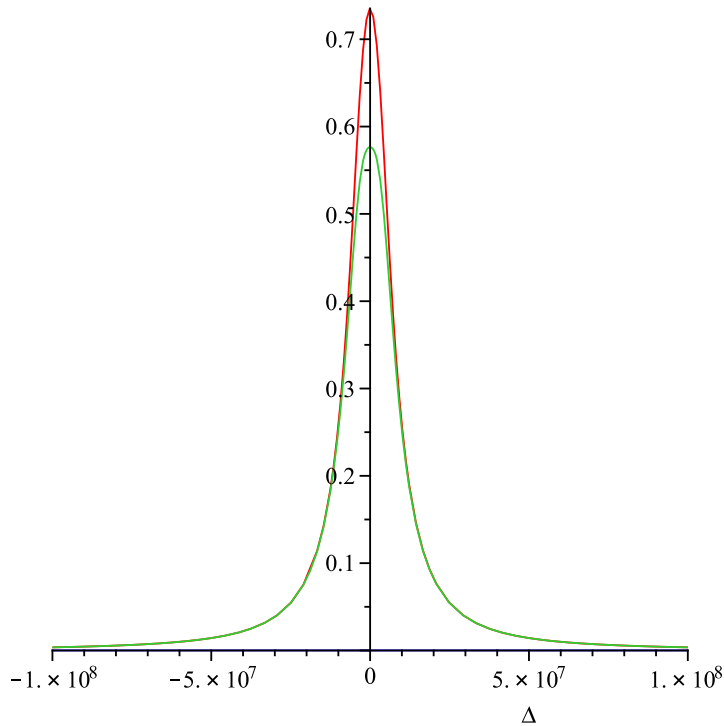


FIG. 1: Calculated values of  $\alpha_+ + \alpha_-$  for varying  $\Delta$  corresponding to a varying laser field frequency given a fixed magnetic. The red curve corresponds to a magnetic field on the order of 300 mG, and the green curve to a magnetic field on order of 700 mG.

The calculated values of  $\alpha_+ + \alpha_-$  (light absorption) for varying one-photon detuning  $\Delta$  are shown in Fig. 1. The resulting curve is the expected absorption of a laser as its frequency is swept through the transition. Note that for greater magnetic field, the absorption is lower. Fig. 2 shows the calculated values of  $kn_+ - kn_-$  for varying  $\Delta$ . The resulting curve is the expected polarization rotation (in radians) of a laser as its frequency is swept through the transition. Maximum rotation is observed when the laser is tuned on optical resonance, and it decreases as the detuning  $\Delta$  increases.

Fig. 3 shows the calculated values of  $\alpha_+ + \alpha_-$  (light absorption) for varying two-photon detuning  $\delta$ . The resulting curve shows reduced absorption of a laser around

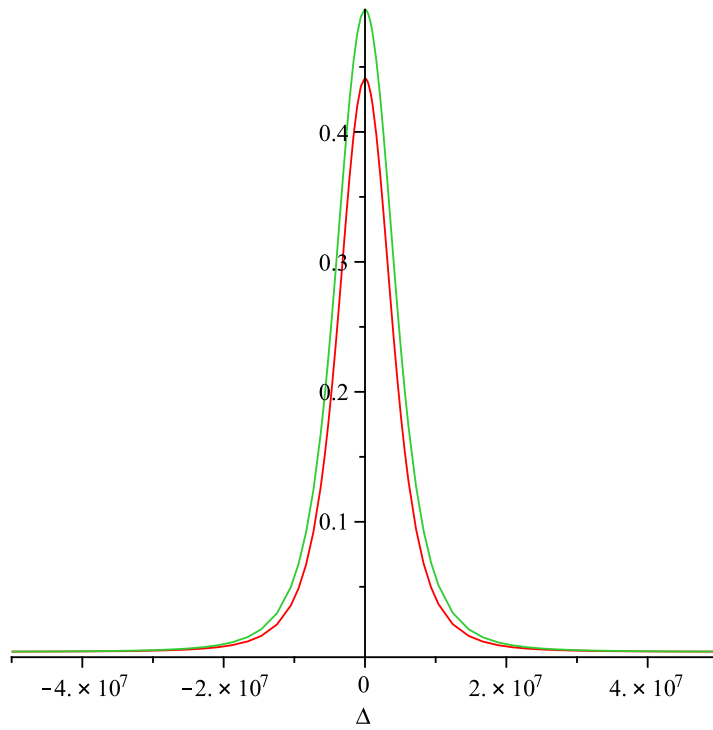


FIG. 2: Calculated values of  $kn_+ - kn_-$  for varying  $\Delta$  corresponding to a varying laser field frequency given a fixed B-field. The red curve corresponds to a magnetic field on the order of 300 mG, and the green curve to a magnetic field on order of 700 mG.

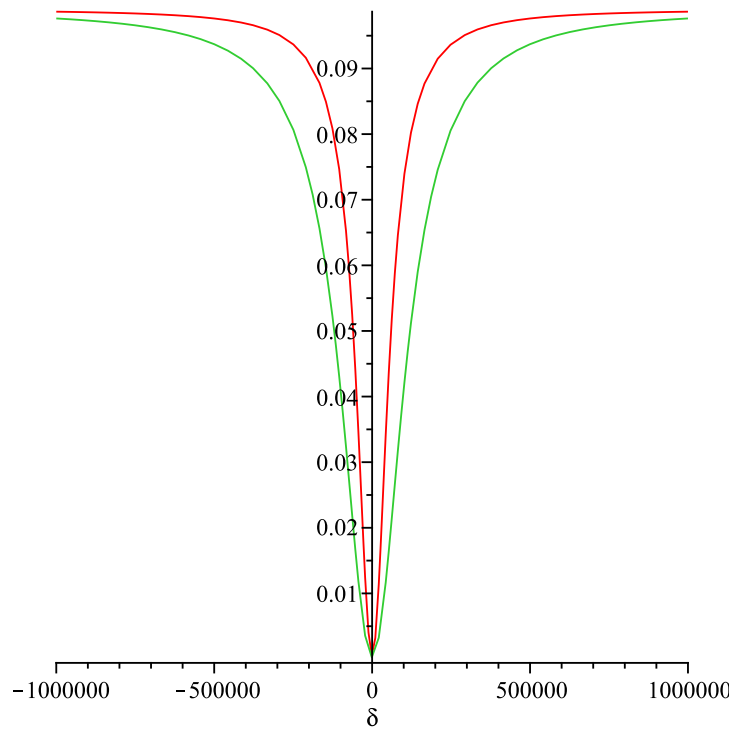


FIG. 3: Calculated values of  $\alpha_+ + \alpha_-$  for varying  $\delta$  corresponding to a varying B-field given a laser field with frequency fixed on a transition. The red curve corresponds to a lower laser power and the green curve to a higher laser power

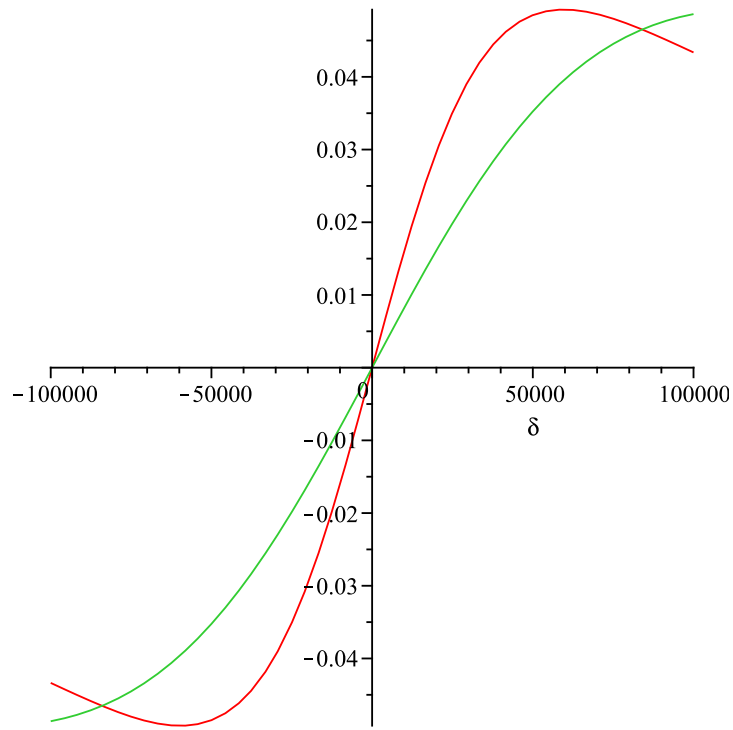


FIG. 4: Calculated values of  $kn_+ - kn_-$  for varying  $\delta$  corresponding to a varying B-field given a laser field with frequency fixed on a transition. The red curve corresponds to a lower laser power and the green curve to a higher laser power

$\delta=0$ , when EIT exists. Fig. 4 shows the calculated values of  $kn_+ - kn_-$  for varying  $\delta$ . The resulting curve is the expected polarization rotation (in radians) of a laser as the magnetic field is swept from positive to negative while the laser is held fixed on the transition. Note that the rotation is much higher for the smaller detuning.

## 2.3 Coated Rb vapor cells

The above calculations do not specify the origin of the ground state decoherence  $\gamma_0$ . For uncoated vapor cells, all coherence is lost in collisions between atoms and cell walls. A paraffin cell coating can mitigate the relaxation effect of wall collisions. In our above theoretical treatment, we have used parameter  $\gamma_0$  to describe the ground-state coherence. For an cell without coating, the effective lifetime  $\frac{1}{\gamma_0}$  is simply the time of flight through the beam path,  $\frac{d}{V}$  for beam of diameter  $d$  and atomic velocity  $V \approx 400 \frac{m}{s}$ . For a coated cell, ground-state coherence lifetime is increased greatly, now being proportional to  $(\frac{D}{V} \cdot N)$  for cell diameter  $D$  and  $N$  the number of wall collisions before decoherence. While the effect has not been modeled analytically, we note that Budker, et al. described and observed a sharper polarization rotation curve around zero magnetic field when using a coated vapor cell in an experiment with a similar setup.[11]

Cell coating is also important when working with multiple lasers aligned parallel to each other without intersecting beam paths, as the increased ground state coherence lifetime greatly increases the probability that atoms will return to the beam path after collision with another atom.

## 3 Procedure

### 3.1 Setup

The initial goal was to reproduce the nonlinear Faraday Effect observed by Sautenkov, et al., in 2000[10]. The experimental setup consists of a laser tuned to the 795 nm  $F = 2 \rightarrow F' = 1$  transition of the  $^{87}\text{Rb}$   $D1$  absorption line. This laser first propagates through a linear polarizer, then through a heated  $^{87}\text{Rb}$  vapor cell with a longitudinal magnetic field, through a  $\frac{\lambda}{2}$  wave plate rotated at a  $22.5^\circ$  angle to incident polarization, and then through a polarizing beam splitter to two photodiodes for measurement.

A magnetic shield, consisting of three nested metal cylinders with an internal mount for a vapor cell, was used. The mount included a thermoelectric cooler (TEC) element to heat the vapor cell, as well as two thermistors to measure the temperature at each end of the cell. Openings existed in the shield on three orthogonal axes permitting laser fields to be propagated through the housed vapor cell. For the experiment the beam path along one axis was designed to accommodate multiple lasers corresponding to multiple Rb resonances, focused into the vapor cell. A commercial External Cavity Diode Laser (ECDL) (Vortex model 6017) tuned to 795 nm, was used in this experiment for initial tests. A second laser, tuned to 780 nm, was aligned parallel to the first laser using an edge mirror, as shown in the schematic in Fig. 5. Its beam was parallel to and close to, but not overlapping the beam of the first laser. At a point after the beams had propagated through the cell and magnetic coil/shield apparatus, a pinhole aperture was introduced such that either beam could be picked

off prior to being sensed at the photodiodes.

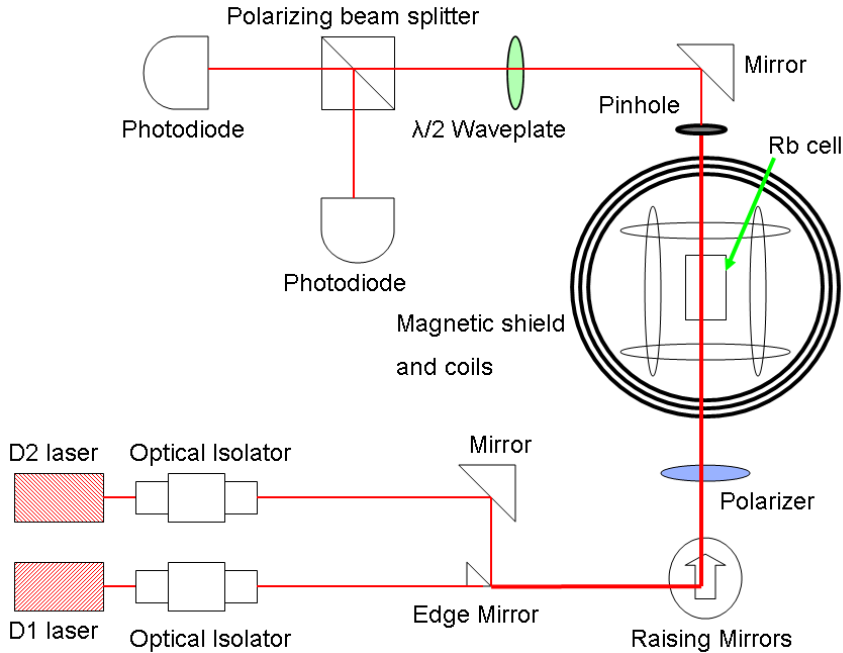


FIG. 5: Schematic of the experimental setup.

### 3.2 Coil Fabrication and Testing

To generate the necessary longitudinal magnetic field for our experiment, some method of generating a homogenous magnetic field inside the magnetic shield had to be implemented. Sautenkov, et. al., made use of a solenoid, however in anticipation of future utilization of multiple axes, a pair of orthogonal Helmholtz coil pairs were designed to allow generation of orthogonal fields and simultaneous use of both axes. The coils were built on a mount designed specifically for our magnetic shield, fabricated from acrylic in order to not create an ambient magnetic field inside the shield. The geometry of Helmholtz coils, with separation between the coils equal to their radius,

necessitates that an orthogonal pair of coil pairs cannot have the same radius. Given an integer number of turns and the equation  $B = \left(\frac{4}{5}\right)^{\frac{3}{2}} \frac{\mu_0 n I}{R}$  for Helmholtz coil field strength, (where  $\mu_0$  is the permeability of free space,  $I$  is the current through the coils,  $R$  is the radius and  $n$  is the number of turns) two orthogonal coil pairs will generate magnetic fields of different strength given the same current. The coils were matched as closely as possible, with one pair of coils having a 17.78 cm radius and 34 turns, and the other pair having a 14.60 cm radius and 28 turns. The result was a calculated  $n/R$  ratio of 4.857 for the larger coil pair and 4.869 for the smaller coil pair.

In order to precisely control the magnetic field, a current amplifier was designed to allow the currents in the coil pairs to be driven by a commercial function generator. The amplifier was designed specifically to be used with the Stanford Research Systems Model DS345 function generator, to operate at frequencies up to 1 kHz, with a maximum current of  $\pm 200$ mA. The current amplifier was based on previously designed MOSFET current amplifiers which operated only in either the positive or negative region. The new design combined the two in an in-feedback push-pull configuration, using pull-up resistors at the transistor gates to eliminate the crossover distortion common in such designs but not acceptable for our use. A schematic of the amplifier is shown in Fig. 6.

After fabrication of the coils and the amplifier, the mounted coils were inserted into the magnetic shield and aligned along the optical axes as governed by the openings in the shield. The magnetic field was tested for both coil pairs using a commercial

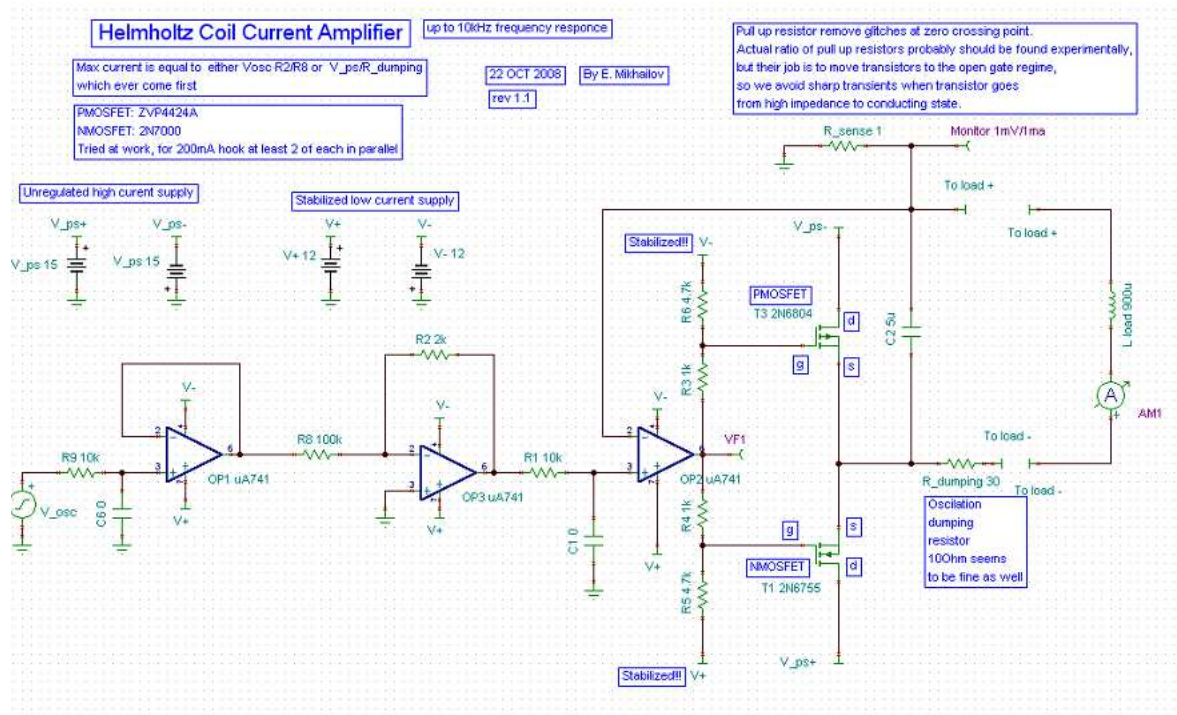


FIG. 6: Current amplifier schematic.

magnetometer (F.W. Bell Model 9500). Both pairs were first tested for magnetic field homogeneity, and were found to be homogenous within the 1 mG accuracy of the magnetometer in an  $64 \text{ cm}^3$  region. Both pairs were then tested to determine magnetic field strength as a function of input voltage. The results (shown in Fig. 7) were linear, as expected, and a linear regression on the data allowed us to determine the functions by which we could calculate magnetic field strength from currents.

While the regressions have high correlation coefficients, ( $R^2$  values) the precision of these regressions will be a subject of future analysis.

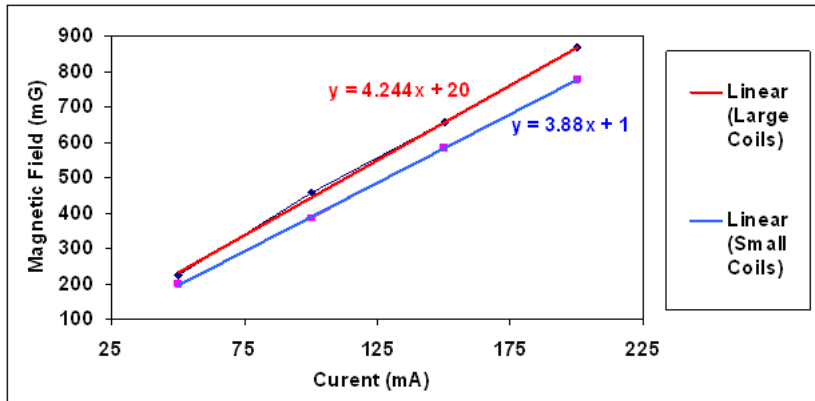


FIG. 7: Magnetic field as a function of current in the orthogonal Helmholtz coil pairs.

### 3.3 Observing the nonlinear Faraday effect

An  $^{87}\text{Rb}$  cell was placed in the cell mount inside the magnetic shield and coil apparatus, and heated to  $\approx 50^\circ\text{C}$ . The 795 nm ECDL was frequency modulated at 40 Hz, to sweep across the transitions of the  $^{87}\text{Rb}$   $D1$  line. A small portion of the beam was split off through a reference cell containing a natural mix of  $^{87}\text{Rb}$  and  $^{85}\text{Rb}$  vapor, to mark the positions of the resonance lines in frequency space. The remainder of the beam was propagated through a linear polarizer and then through the  $^{87}\text{Rb}$  cell inside the magnetic shield. After propagating through  $^{87}\text{Rb}$  cell, the beam was passed through a  $\frac{\lambda}{2}$  waveplate  $22.5^\circ$  to incident polarization. The beam was then split with a polarizing beam splitter, into two components, which have intensities given in equations:

$$I_1 = \frac{1}{2}I + \frac{1}{2}I\sin(2\phi) \quad (24)$$

$$I_2 = \frac{1}{2}I - \frac{1}{2}I\sin(2\phi) \quad (25)$$

where  $I$  is the incident intensity of the beam and  $\phi$  is the rotation angle. Each component's intensity is measured using a photodiode. The rotation angle through the  $^{87}\text{Rb}$  cell can then be determined using the following equation.

$$\phi = \frac{1}{2} \sin^{-1} \left( \frac{I_1 - I_2}{I_1 + I_2} \right) \quad (26)$$

A circuit containing two subtracting photodiodes was used for this application, as the data of most importance was the difference in intensity and the subtracting circuit reduced the effects that variations in overall laser intensity might have on the data had two independently-sampling photodiodes been used. This procedure was conducted both with no magnetic field present and with a static longitudinal magnetic field corresponding to  $\pm 200\text{mA}$  and  $\pm 50\text{mA}$  run through the coils. These fields had corresponding strengths of  $\pm 850\text{mG}$  and  $\pm 340\text{mG}$  based on previous analysis of field strength as a function of current. The procedure was conducted with both a high laser power ( $185 \mu\text{W}$ ) and a low laser power ( $85 \mu\text{W}$ ) as measured by a commercial optical power meter (ILX Lightwave OMM-6810B). The data for  $I_1$  and  $I_2$  were analysed using equation (26) to obtain rotation angle ( $\phi$ ) The results for the  $185 \mu\text{W}$  and  $85 \mu\text{W}$  laser powers are shown in Fig. 8 and Fig. 9 respectively.

The position of the rotation peaks in frequency space was determined relative to the  $F=2 \rightarrow F'=1$   $^{87}\text{Rb}$  line using data recorded from the reference cell. Fig. 10 shows data taken from the reference cell. Note how in Figs. 8 and 9 that the rotation angle increases around transitions, proportional in magnitude to the applied magnetic field.

This matches our expectations from theoretical results (compare to Fig. 2. in the theory section). Note also that the reference cell contains both  $^{87}\text{Rb}$  as well as  $^{85}\text{Rb}$ , and some of the absorption resonances observed in the reference cell do not appear in main cell rotation curve, as the main cell contains only  $^{87}\text{Rb}$ .

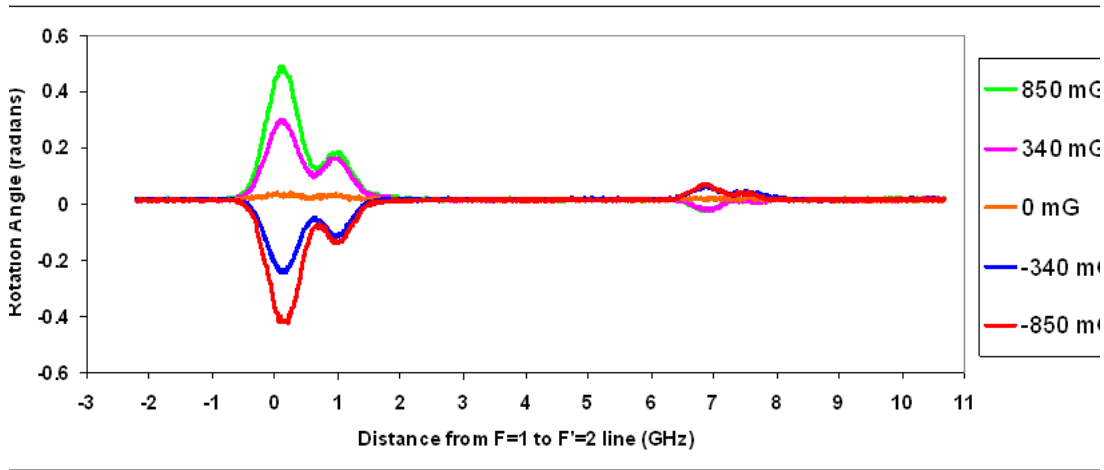


FIG. 8: Rotation angle through the  $^{87}\text{Rb}$  vapor cell with respect to frequency for longitudinal magnetic fields of varying strength and D1 laser power of  $185 \mu\text{W}$ .

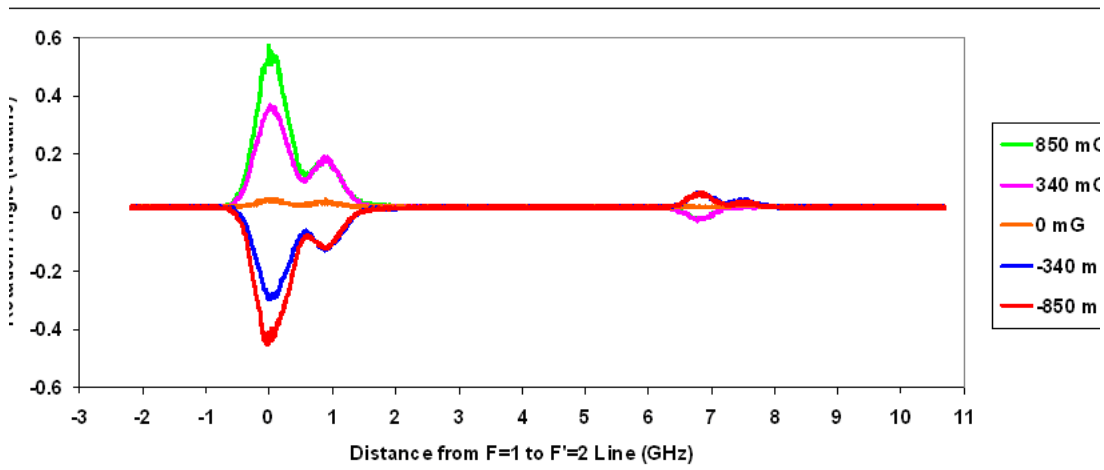


FIG. 9: Rotation angle through the  $^{87}\text{Rb}$  vapor cell with respect to frequency for longitudinal magnetic fields of varying strength and D1 laser power of  $85 \mu\text{W}$ .

This procedure was then repeated, substituting a transverse magnetic field for the

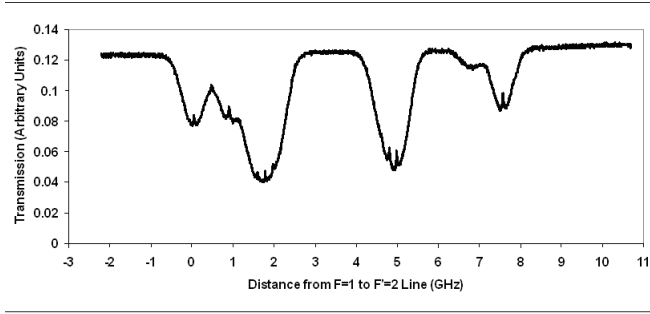


FIG. 10: Data from the reference  $^{87}\text{Rb}$  and  $^{85}\text{Rb}$  vapor cell, used to determine the relative location in frequency space of the other recorded data.

longitudinal magnetic field. Due to the differences in Helmholtz coil size, the same  $\pm 200$  mA and  $\pm 50$  mA currents yielded slightly lower magnetic field strengths, as shown in Fig. 6. The rotation angle was calculated using equation (26), and the results are shown in Fig. 11. Because the effect is much smaller for transverse fields, only the higher laser power ( $185 \mu\text{W}$ ) was used. Note, however, that the data for longitudinal fields matched with the expected values we determined earlier analytically, with maximum polarization rotation occurring near each of the transitions, and rotation falling off as distance from the transition increases.

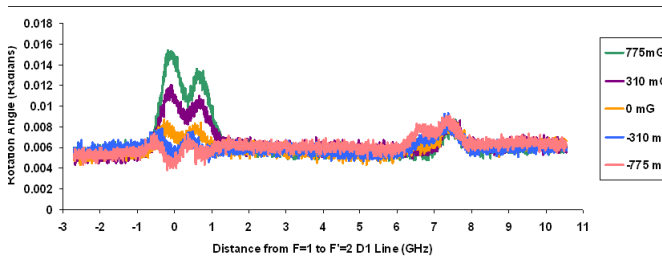


FIG. 11: Rotation angle through the  $^{87}\text{Rb}$  vapor cell with respect to frequency for transverse magnetic fields of varying strength and D1 laser power of  $185 \mu\text{W}$ .

The frequency of the ECDL was then tuned to the  $F=2 \rightarrow F'=1$   $^{87}\text{Rb}$  line and held constant, while the magnetic field was swept between  $+1020$  mG and  $-1000$  mG

at 40 Hz. The rotation angle was recorded, and this procedure was repeated for measured laser powers of  $85 \mu\text{W}$  and  $185 \mu\text{W}$ . Fig. 12 shows a comparison between the rotation angle and the magnetic field for the two different laser powers. This behavior matches precisely the curve determined theoretically, and shown in Fig. 4. Note that due to our inability to sweep the magnetic fields beyond certain maximum absolute amplitudes, our experimental curve does not extend as far to the sides as the curve in Fig. 4., but are valid in the inner, near-zero magnetic field region for which we were able to collect data. Rotation is greater in the area near zero magnetic field for the lower laser power, which also agrees with our theoretical calculations.

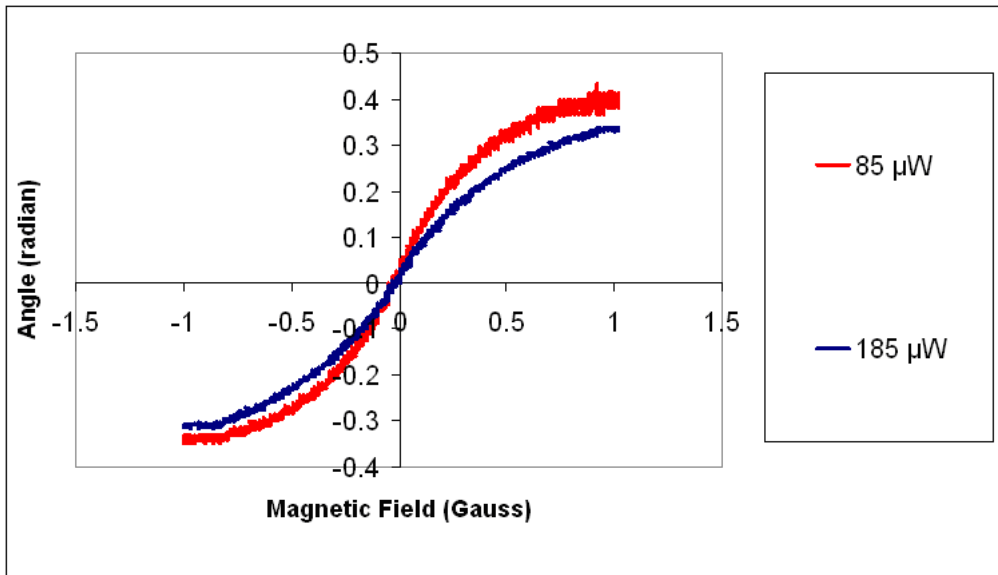


FIG. 12: Polarization rotation angle of a laser tuned to the  $F=1 \rightarrow F'=2$   $^{87}\text{Rb}$  line with powers of  $85 \mu\text{W}$  and  $185 \mu\text{W}$  and propagated through  $^{87}\text{Rb}$  vapor cell as a function of magnetic field

Measurements for constant longitudinal magnetic field with variable laser frequency and sweeping longitudinal magnetic field with fixed laser frequency were repeated using a laser tuned to 780 nm, corresponding to the D2 line of Rb. Since the rotation effect

for the D2 transitions is less than that for the D1 transitions, no measurements with transverse magnetic fields were recorded. Data for measurements of rotation angle with several constant magnetic fields with the laser frequency modulated at 40 Hz is shown in Fig. 13. Data for measurements with the laser tuned to the F=1 transitions and a sweeping magnetic field is shown in Fig. 14. Once again, these data for the D2 line match our calculated values as the data from the D1 line did. The curve, compared to the experimental curve (in Fig. 4) does not extend as far to the sides due to the limitations of our ability to generate magnetic fields, but the rotation near zero magnetic field mimics the experimental data well, with rotation again being greater for the lower laser power.

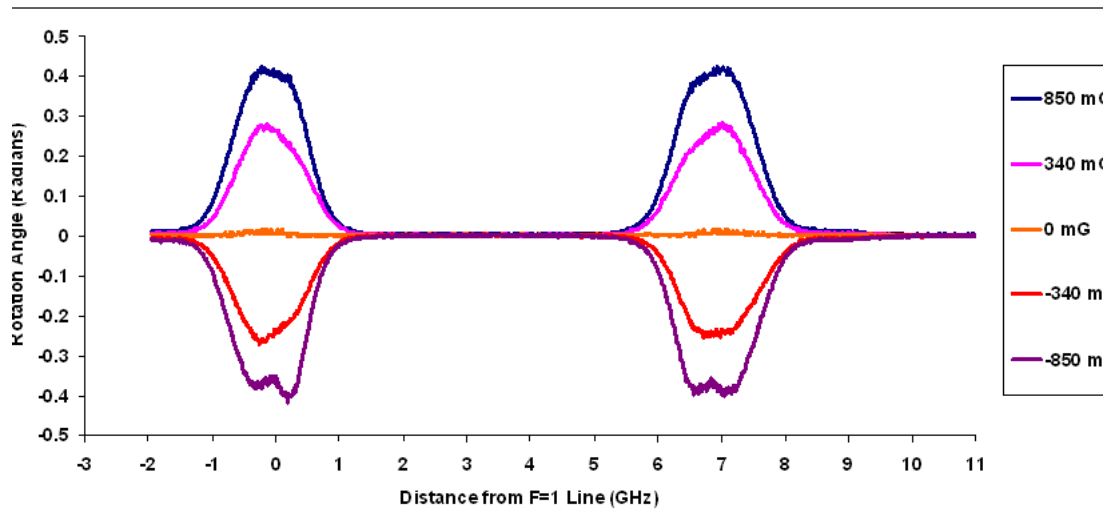


FIG. 13: Rotation angle through the  $^{87}\text{Rb}$  vapor cell with respect to frequency for longitudinal magnetic fields of varying strength and D2 laser power of 1130 mW.

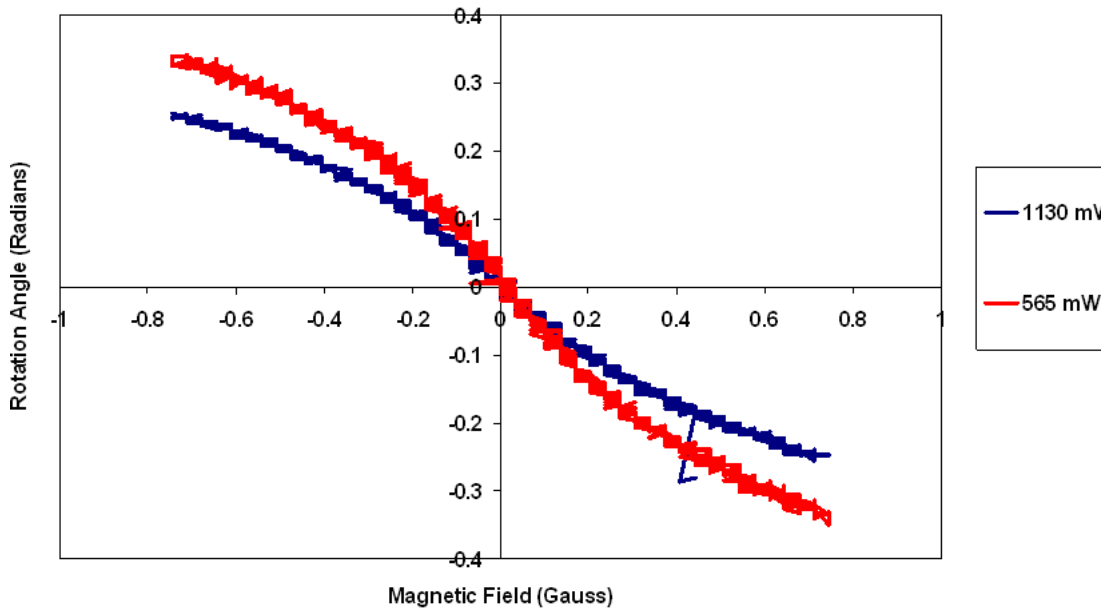


FIG. 14: Polarization rotation angle of a laser tuned to the F=1 D2 Rb transitions with powers of 565mW and 1130mW and propagated through  $^{87}\text{Rb}$  vapor cell as a function of magnetic field

### 3.4 Observations using a coated Rb cell

All previous measurements were taken using the uncoated vapor cell containing only  $^{87}\text{Rb}$ . A vapor cell with the paraffin coating and containing both  $^{85}\text{Rb}$  and  $^{87}\text{Rb}$  was substituted into the magnetic shield/coil chamber. The walls of the  $^{85}\text{Rb}$  and  $^{87}\text{Rb}$  cell were coated with paraffin, a technique that has been found to extend coherence lifetime by reducing the effect of wall-collisions on decoherence[12]. As outlined in section 2, we expected the applied magnetic field to have a stronger effect on polarization rotation near zero magnetic field than for an uncoated cell, with the effect on polarization rotation becoming similar to that of an uncoated cell for larger absolute values of the applied magnetic field.

Data of polarization rotation as a function of magnetic field taken using the coated

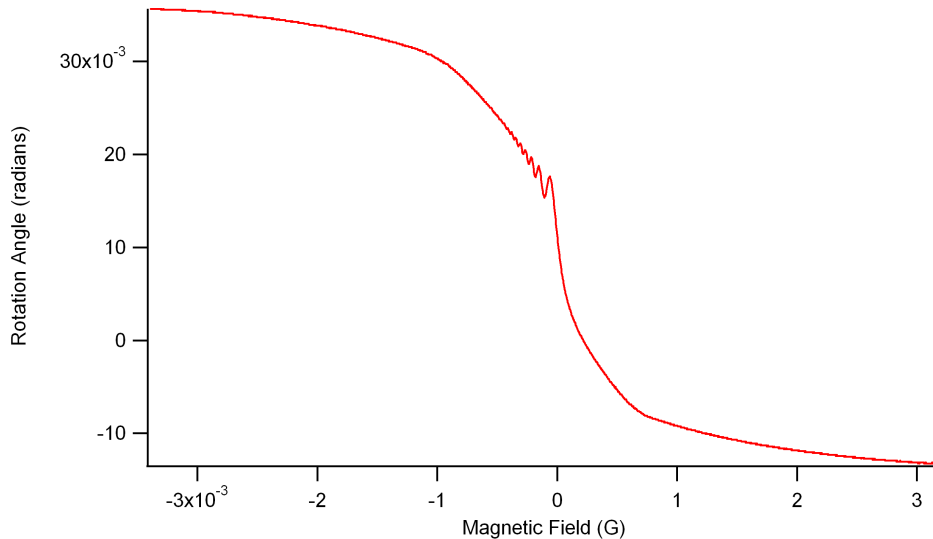


FIG. 15: Polarization rotation angle of a laser tuned to the  $F=1 \rightarrow F'=2$   $^{87}\text{Rb}$  line and propagated through a coated  $^{85}\text{Rb}$  and  $^{87}\text{Rb}$  cell with a sweeping magnetic field

cell, shown in Fig. 15. As expected, the slope of the polarization rotation curve is steeper near zero magnetic field than for larger magnetic field values. Compare to the smooth rotation curves near zero magnetic field in Figs. 12 and 14, which are data from an uncoated cell. Like polarization rotation in an uncoated cell, this effect has already been demonstrated, but its existence confirms that the cell coating is working to increase the coherence time of the Rb atoms. This is important for investigating collisional transfer as the increased coherence time increases the likelihood of an atom returning to the beam path after colliding with another atom.

### 3.5 Combination of D1 and D2 lasers

A second laser, tuned to the 780 nm  $^{87}\text{Rb}$   $D2$  absorption line, was aligned parallel to the first laser using an edge mirror. The spacing was such that both lasers were

propagated through the shielded  $^{87}\text{Rb}$  cell, but that the D1 laser was blocked prior to measurement at the photodiodes. This permitted us to observe the effect the D1 laser had on the polarization rotation of the D2 laser.

As the D1 laser was (for laser model-specific reasons) more precisely controllable, the D2 laser was fixed to an atomic transition of Rb and the D1 laser was swept linearly across a range of frequencies. Several rotation traces were recorded to eliminate systematic errors. First the D1 laser was operated without the D2 laser to ensure that there was no transmission of the D1 laser. The D2 laser was then operated without the D1 laser, sweeping the magnetic field such that by observing the polarization rotation, the laser could be tuned as closely as possible to an atomic transition of Rb. Once the D2 laser was fixed on a transition, the magnetic field was disabled and the D1 laser was operated, sweeping linearly. The magnetic field was then fixed at 25 mG, with the D2 laser still fixed on a transition and the D1 laser sweeping. This was repeated with a magnetic field fixed at -25mG. The resulting polarization rotations are visible in Fig. 16. When a magnetic field is applied, polarization rotation is much greater, and aligned with atomic transitions as displayed by the reference cell, indicating that there is some effect from the D1 laser on the polarization rotation of the D2 laser only when EIT occurs. It is crucial to note that at this time, with no theoretical treatment of collisional transfer of coherence, it is impossible to determine whether or not any of the visible effect is due to collisional transfer or not. There are other causes, such as repopulation of D2 states by the D1 laser, that could be responsible for the observed effect. There is also a general amplitude shift of the

polarization rotation for the varying levels of magnetic field. At this time it cannot be determined if this amplitude shift is the result of a physical effect or not due to an instability in our experimental setup. This will be discussed further in the following section.

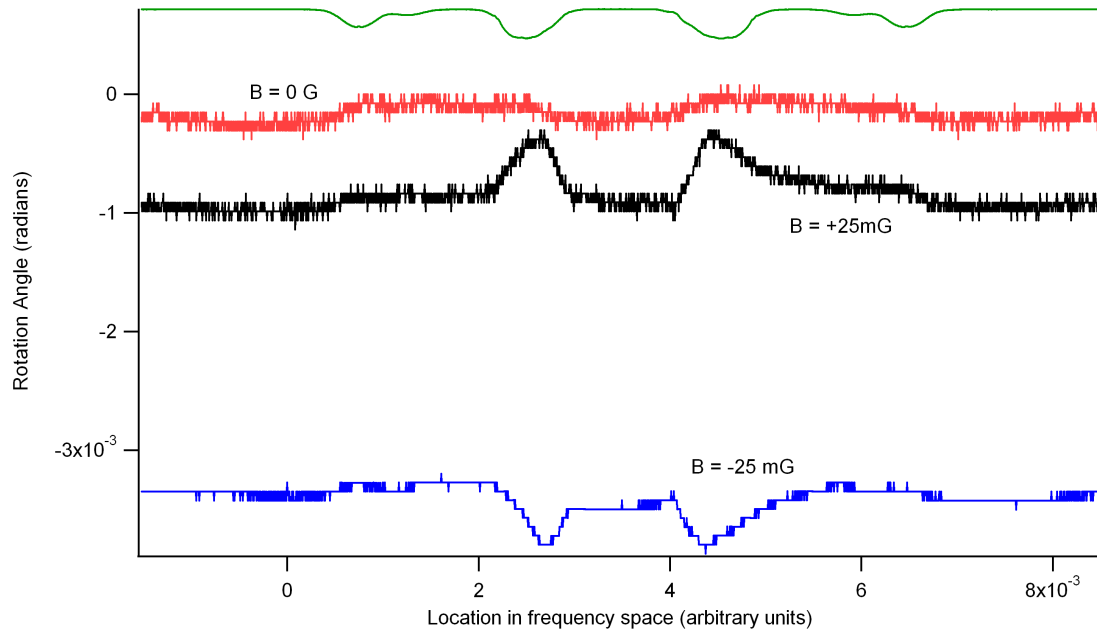


FIG. 16: Polarization rotation of D2 laser propagated through  $^{85}\text{Rb}$  and  $^{87}\text{Rb}$  cell with varying amplitudes of fixed magnetic field and D1 laser frequency sweeping linearly. Data from the  $^{85}\text{Rb}$  and  $^{87}\text{Rb}$  reference cell is displayed above to provide frequency reference.

## 4 Conclusions and Future Work

Our data confirms the observation of the nonlinear Faraday effect in the coated cell, and the observation of some effect of one laser on the polarization rotation of a second one. This indicates our setup is appropriate for use in examining the effects of collisional transfer on coherence lifetime in future experiments. While it is notable that we have been able to observe the effects of one laser on the polarization rotation of another, it will be important to characterize theoretically the expected effects of collisional transfer on rotation.

The experimental setup itself still requires some modification in the areas of signal processing and stabilization. Currently, data acquisition is limited by the resolution of our oscilloscopes in conjunction with the magnitude of the signal output by the photodiodes used. This is visible clearly in Fig. 16 in the low resolution of the polarization rotation for the laser with -25 mG magnetic field applied. Reducing any attenuation processed at the photodiodes will help to increase our useful resolution for taking data.

In addition, the experiment has been pervaded by issues with laser amplitude stability, which greatly hinder our ability to deal with the former problem simply through the addition of a "gain" stage, as linear amplification of an unstable signal amplifies the instability. This instability causes great variance in the magnitude of the  $I_1 + I_2$  signal in equation (19). As mentioned in the previous section and clearly visible in Fig. 16, the amplitude with respect to frequency of our data is not affected,

as each "set" of data (in our case, the data for rotation with respect to frequency for a single magnetic field amplitude) is acquired much more quickly than the rate at which the instability occurs. Unfortunately, data set-to-set is affected significantly by this instability, resulting in the random offset of the rotation-vs.-frequency curves in Fig. 16. The stability issue can be addressed in a series of ways. At the time of this writing, the optical table's pneumatic damping legs had not yet been pressurized, a step which may increase the stability of our laser amplitudes. In addition, certain specific elements involved in physically raising the beam (a necessary step for using our magnetic shield/coil apparatus) have a demonstrated destabilizing effect on the beam's amplitude, and a careful reconstruction of this stage may yield a more stable signal. Finally, the current method of combining the D1 and D2 laser beams with an edge mirror may produce more instability than a method using polarizers and beam splitters.

## References

- [1] D. P. DiVincenzo, "The Physical Implementation of Quantum Computation," *Fortschritte der Physik*, (2000)
- [2] M. Fleischhauer and M. D. Lukin, "Quantum memory for photons: Dark-state polaritons," *Phys. Rev. A* 65 022314 (2002)
- [3] B. Julsgaard, J. Sherson, J. I. Cirac, J. Fiurasek, and E. S. Polzik, "Experimental demonstration of quantum memory for light," *Nature (London)* 432, 482 (2004).
- [4] N. B. Phillips, A. V. Gorshkov, and I. Novikova, "Optimal light storage in atomic vapor," *Phys. Rev. A* 78, 020302 (2008).
- [5] I. Novikova, A. V. Gorshkov, D. F. Phillips, A. S. Sorensen, M. D. Lukin, and R. L. Walsworth, "Optimal Control of Light Pulse Storage and Retrieval," *Phys. Rev. Lett.* 98, 243602 (2007).
- [6] W. Happer, "Optical Pumping," *Rev. Mod. Phys.* 44, 169 (1972)
- [7] S.E. Harris, Electromagnetically Induced Transparency, *Phys. Today* 50(7), 36-41 (1997).
- [8] D. F. Phillips, A. Fleischhauer, A. Mair, R. L. Walsworth, and M. D. Lukin, Storage of Light in Atomic Vapor, *Phys. Rev. Lett.* 86, 783-786 (2001).

- [9] B. Kraus, W. Tittel, N. Gisin, M. Nilsson, S. Kroll, and J. I. Cirac, Quantum memory for nonstationary light fields based on controlled reversible inhomogeneous broadening, *Phys. Rev. A* 73, 020302 (2006).
- [10] V. A. Sautenkov, M. D. Lukin, C. J. Bednar, I. Novikova, E. Mikhailov, M. Fleischauer, V. L. Velichansky, G.R. Welch, and M. O. Scully, "Enhancement of magneto-optic effects via large atomic coherence in optically dense media," *Phys. Rev. A* 62, 023810 (2000)
- [11] D. Budker, V. Yashchuk, and M. Zolotarev, "Nonlinear Magneto-optic Effects with Ultranarrow Widths," *Phys. Rev. Lett.* 81, 5788-5791 (1998).
- [12] V.V. Yashchuk, E. Mikhailov, I. Novikova, D. Budker, D. F. Kimball, and M. Zolotarev, "Nonlinear magneto-optical rotation with separated light fields in  $^{85}\text{Rb}$  vapor contained in an anti-relaxation coated cell," preprint LBNL-44762 (1999).
- [13] T.G. Walker, and W. Happer, "Spin-exchange optical pumping of noble-gas nuclei," *Rev. Mod. Phys.* 69, 629 - 642 (1997).